Research Article | Vol. 9, No. 1 | 1 Jan 2018 | BIOMEDICAL OPTICS EXPRESS 214
Biomedical Optics EXPRESS

Label-free imaging of atherosclerotic plaques using third-harmonic generation microscopy

DAVID M. SMALL,[1,3] JASON S. JONES,[1,3] IRWIN I. TENDLER,[1] PAUL E. MILLER,[2] ANDRE GHETTI,[2] AND NOZOMI NISHIMURA[1,*]

[1]*Nancy E. and Peter C. Meinig School of Biomedical Engineering, Cornell University, 526 N. Campus Rd., Ithaca, NY 14853, USA*
[2]*Anabios Corporation, 3030 Bunker Hill St., San Diego, CA 92109, USA*
[3]*Contributed equally*
[*]*nn62@cornell.edu*

Abstract: Multiphoton microscopy using laser sources in the mid-infrared range (MIR, 1,300 nm and 1,700 nm) was used to image atherosclerotic plaques from murine and human samples. Third harmonic generation (THG) from atherosclerotic plaques revealed morphological details of cellular and extracellular lipid deposits. Simultaneous nonlinear optical signals from the same laser source, including second harmonic generation and endogenous fluorescence, resulted in label-free images of various layers within the diseased vessel wall. The THG signal adds an endogenous contrast mechanism with a practical degree of specificity for atherosclerotic plaques that complements current nonlinear optical methods for the investigation of cardiovascular disease. Our use of whole-mount tissue and backward scattered epi-detection suggests THG could potentially be used in the future as a clinical tool.

OCIS codes: (170.3880) Medical and biological imaging; (180.4315) Nonlinear microscopy; (170.6935) Tissue characterization.

References and links

1. H. C. Stary, A. B. Chandler, R. E. Dinsmore, V. Fuster, S. Glagov, W. Insull, Jr., M. E. Rosenfeld, C. J. Schwartz, W. D. Wagner, and R. W. Wissler, "A definition of advanced types of atherosclerotic lesions and a histological classification of atherosclerosis. A report from the Committee on Vascular Lesions of the Council on Arteriosclerosis, American Heart Association," Circulation **92**(5), 1355–1374 (1995).
2. H. C. Stary, A. B. Chandler, S. Glagov, J. R. Guyton, W. Insull, Jr., M. E. Rosenfeld, S. A. Schaffer, C. J. Schwartz, W. D. Wagner, and R. W. Wissler, "A definition of initial, fatty streak, and intermediate lesions of atherosclerosis. A report from the Committee on Vascular Lesions of the Council on Arteriosclerosis, American Heart Association," Circulation **89**(5), 2462–2478 (1994).
3. D. Mozaffarian, E. J. Benjamin, A. S. Go, D. K. Arnett, M. J. Blaha, M. Cushman, S. de Ferranti, J. P. Després, H. J. Fullerton, V. J. Howard, M. D. Huffman, S. E. Judd, B. M. Kissela, D. T. Lackland, J. H. Lichtman, L. D. Lisabeth, S. Liu, R. H. Mackey, D. B. Matchar, D. K. McGuire, E. R. Mohler 3rd, C. S. Moy, P. Muntner, M. E. Mussolino, K. Nasir, R. W. Neumar, G. Nichol, L. Palaniappan, D. K. Pandey, M. J. Reeves, C. J. Rodriguez, P. D. Sorlie, J. Stein, A. Towfighi, T. N. Turan, S. S. Virani, J. Z. Willey, D. Woo, R. W. Yeh, and M. B. Turner; American Heart Association Statistics Committee and Stroke Statistics Subcommittee, "Heart disease and stroke statistics--2015 update: a report from the American Heart Association," Circulation **131**(4), e29–e322 (2015).
4. G. K. Hansson, "Inflammation, atherosclerosis, and coronary artery disease," N. Engl. J. Med. **352**(16), 1685–1695 (2005).
5. M. A. Latif and M. J. Budoff, "Role of CT angiography for detection of coronary atherosclerosis," Expert Rev. Cardiovasc. Ther. **12**(3), 373–382 (2014).
6. A. Thomassen, H. Petersen, A. C. Diederichsen, H. Mickley, L. O. Jensen, A. Johansen, O. Gerke, P. E. Braad, P. Thayssen, M. M. Høilund-Carlsen, W. Vach, J. Knuuti, and P. F. Høilund-Carlsen, "Hybrid CT angiography and quantitative 15O-water PET for assessment of coronary artery disease: comparison with quantitative coronary angiography," Eur. J. Nucl. Med. Mol. Imaging **40**(12), 1894–1904 (2013).
7. D. D. Adraktas, E. Tong, A. D. Furtado, S. C. Cheng, and M. Wintermark, "Evolution of CT imaging features of carotid atherosclerotic plaques in a 1-year prospective cohort study," J. Neuroimaging **24**(1), 1–6 (2014).
8. R. Corti and V. Fuster, "Imaging of atherosclerosis: magnetic resonance imaging," Eur. Heart J. **32**(14), 1709–1719 (2011).
9. C. Yuan, L. M. Mitsumori, M. S. Ferguson, N. L. Polissar, D. Echelard, G. Ortiz, R. Small, J. W. Davies, W. S. Kerwin, and T. S. Hatsukami, "In vivo accuracy of multispectral magnetic resonance imaging for identifying

#307722 https://doi.org/10.1364/BOE.9.000214
Journal © 2018 Received 22 Sep 2017; revised 24 Nov 2017; accepted 2 Dec 2017; published 13 Dec 2017

Biomedical Optics EXPRESS

lipid-rich necrotic cores and intraplaque hemorrhage in advanced human carotid plaques," Circulation **104**(17), 2051–2056 (2001).
10. Z. A. Fayad, T. Nahar, J. T. Fallon, M. Goldman, J. G. Aguinaldo, J. J. Badimon, M. Shinnar, J. H. Chesebro, and V. Fuster, "In vivo magnetic resonance evaluation of atherosclerotic plaques in the human thoracic aorta: a comparison with transesophageal echocardiography," Circulation **101**(21), 2503–2509 (2000).
11. K. W. Moon, J. H. Kim, K. D. Yoo, S. S. Oh, D. B. Kim, and C. M. Kim, "Evaluation of radial artery atherosclerosis by intravascular ultrasound," Angiology **64**(1), 73–79 (2013).
12. D. Böse, C. von Birgelen, and R. Erbel, "Intravascular ultrasound for the evaluation of therapies targeting coronary atherosclerosis," J. Am. Coll. Cardiol. **49**(9), 925–932 (2007).
13. J. Ge, F. Chirillo, J. Schwedtmann, G. Görge, M. Haude, D. Baumgart, V. Shah, C. von Birgelen, S. Sack, H. Boudoulas, and R. Erbel, "Screening of ruptured plaques in patients with coronary artery disease by intravascular ultrasound," Heart **81**(6), 621–627 (1999).
14. H. G. Bezerra, M. A. Costa, G. Guagliumi, A. M. Rollins, and D. I. Simon, "Intracoronary optical coherence tomography: a comprehensive review clinical and research applications," JACC Cardiovasc. Interv. **2**(11), 1035–1046 (2009).
15. H. Yabushita, B. E. Bouma, S. L. Houser, H. T. Aretz, I. K. Jang, K. H. Schlendorf, C. R. Kauffman, M. Shishkov, D. H. Kang, E. F. Halpern, and G. J. Tearney, "Characterization of human atherosclerosis by optical coherence tomography," Circulation **106**(13), 1640–1645 (2002).
16. A. Tanaka, T. Imanishi, H. Kitabata, T. Kubo, S. Takarada, H. Kataiwa, A. Kuroi, H. Tsujioka, T. Tanimoto, N. Nakamura, M. Mizukoshi, K. Hirata, and T. Akasaka, "Distribution and frequency of thin-capped fibroatheromas and ruptured plaques in the entire culprit coronary artery in patients with acute coronary syndrome as determined by optical coherence tomography," Am. J. Cardiol. **102**(8), 975–979 (2008).
17. R. B. Singh, S. A. Mengi, Y. J. Xu, A. S. Arneja, and N. S. Dhalla, "Pathogenesis of atherosclerosis: A multifactorial process," Exp. Clin. Cardiol. **7**(1), 40–53 (2002).
18. R. M. Boyd, *Nonlinear Optics,* 3rd ed. (Wiley, 2008).
19. R. F. Barth, D. A. Kellough, P. Allenby, L. E. Blower, S. H. Hammond, G. M. Allenby, and L. M. Buja, "Assessment of atherosclerotic luminal narrowing of coronary arteries based on morphometrically generated visual guides," Cardiovasc. Pathol. **29**, 53–60 (2017).
20. J. Wang, C. Sun, N. Gerdes, C. Liu, M. Liao, J. Liu, M. A. Shi, A. He, Y. Zhou, G. K. Sukhova, H. Chen, X. W. Cheng, M. Kuzuya, T. Murohara, J. Zhang, X. Cheng, M. Jiang, G. E. Shull, S. Rogers, C. L. Yang, Q. Ke, S. Jelen, R. Bindels, D. H. Ellison, P. Jarolim, P. Libby, and G. P. Shi, "Interleukin 18 function in atherosclerosis is mediated by the interleukin 18 receptor and the Na-Cl co-transporter," Nat. Med. **21**(7), 820–826 (2015).
21. I. Perrotta, "Ultrastructural features of human atherosclerosis," Ultrastruct. Pathol. **37**(1), 43–51 (2013).
22. I. A. Sobenin, M. A. Sazonova, A. Y. Postnov, Y. V. Bobryshev, and A. N. Orekhov, "Changes of mitochondria in atherosclerosis: possible determinant in the pathogenesis of the disease," Atherosclerosis **227**(2), 283–288 (2013).
23. W. R. Zipfel, R. M. Williams, and W. W. Webb, "Nonlinear magic: multiphoton microscopy in the biosciences," Nat. Biotechnol. **21**(11), 1369–1377 (2003).
24. W. R. Zipfel, R. M. Williams, R. Christie, A. Y. Nikitin, B. T. Hyman, and W. W. Webb, "Live tissue intrinsic emission microscopy using multiphoton-excited native fluorescence and second harmonic generation," Proc. Natl. Acad. Sci. U.S.A. **100**(12), 7075–7080 (2003).
25. R. Carriles, D. N. Schafer, K. E. Sheetz, J. J. Field, R. Cisek, V. Barzda, A. W. Sylvester, and J. A. Squier, "Invited review article: Imaging techniques for harmonic and multiphoton absorption fluorescence microscopy," Rev. Sci. Instrum. **80**(8), 081101 (2009).
26. N. Nishimura, C. B. Schaffer, B. Friedman, P. S. Tsai, P. D. Lyden, and D. Kleinfeld, "Targeted insult to subsurface cortical blood vessels using ultrashort laser pulses: three models of stroke," Nat. Methods **3**(2), 99–108 (2006).
27. D. G. Ouzounov, T. Wang, M. Wang, D. D. Feng, N. G. Horton, J. C. Cruz-Hernández, Y. T. Cheng, J. Reimer, A. S. Tolias, N. Nishimura, and C. Xu, "In vivo three-photon imaging of activity of GCaMP6-labeled neurons deep in intact mouse brain," Nat. Methods **14**(4), 388–390 (2017).
28. N. Nishimura, C. B. Schaffer, B. Friedman, P. D. Lyden, and D. Kleinfeld, "Penetrating arterioles are a bottleneck in the perfusion of neocortex," Proc. Natl. Acad. Sci. U.S.A. **104**(1), 365–370 (2007).
29. D. M. Small, W. Y. Sanchez, S. Roy, M. J. Hickey, and G. C. Gobe, "Multiphoton fluorescence microscopy of the live kidney in health and disease," J. Biomed. Opt. **19**(2), 020901 (2014).
30. C. Auffray, D. Fogg, M. Garfa, G. Elain, O. Join-Lambert, S. Kayal, S. Sarnacki, A. Cumano, G. Lauvau, and F. Geissmann, "Monitoring of blood vessels and tissues by a population of monocytes with patrolling behavior," Science **317**(5838), 666–670 (2007).
31. A. D. Aguirre, C. Vinegoni, M. Sebas, and R. Weissleder, "Intravital imaging of cardiac function at the single-cell level," Proc. Natl. Acad. Sci. U.S.A. **111**(31), 11257–11262 (2014).
32. D. Débarre, W. Supatto, and E. Beaurepaire, "Structure sensitivity in third-harmonic generation microscopy," Opt. Lett. **30**(16), 2134–2136 (2005).
33. D. Débarre, W. Supatto, A. M. Pena, A. Fabre, T. Tordjmann, L. Combettes, M. C. Schanne-Klein, and E. Beaurepaire, "Imaging lipid bodies in cells and tissues using third-harmonic generation microscopy," Nat. Methods **3**(1), 47–53 (2006).

Biomedical Optics EXPRESS

34. G. Bautista, S. G. Pfisterer, M. J. Huttunen, S. Ranjan, K. Kanerva, E. Ikonen, and M. Kauranen, "Polarized THG microscopy identifies compositionally different lipid droplets in mammalian cells," Biophys. J. **107**(10), 2230–2236 (2014).
35. M. J. Farrar, F. W. Wise, J. R. Fetcho, and C. B. Schaffer, "In vivo imaging of myelin in the vertebrate central nervous system using third harmonic generation microscopy," Biophys. J. **100**(5), 1362–1371 (2011).
36. Y. C. Chen, H. C. Hsu, C. M. Lee, and C. K. Sun, "Third-harmonic generation susceptibility spectroscopy in free fatty acids," J. Biomed. Opt. **20**(9), 095013 (2015).
37. M. Seeger, A. Karlas, D. Soliman, J. Pelisek, and V. Ntziachristos, "Multimodal optoacoustic and multiphoton microscopy of human carotid atheroma," Photoacoustics **4**(3), 102–111 (2016).
38. H. C. Stary, A. B. Chandler, S. Glagov, J. R. Guyton, W. Insull, Jr., M. E. Rosenfeld, S. A. Schaffer, C. J. Schwartz, W. D. Wagner, and R. W. Wissler, "A definition of initial, fatty streak, and intermediate lesions of atherosclerosis. A report from the Committee on Vascular Lesions of the Council on Arteriosclerosis, American Heart Association," Arterioscler. Thromb. **14**(5), 840–856 (1994).
39. K. S. Meir and E. Leitersdorf, "Atherosclerosis in the apolipoprotein-E-deficient mouse: a decade of progress," Arterioscler. Thromb. Vasc. Biol. **24**(6), 1006–1014 (2004).
40. D. A. Tulis, "Histological and morphometric analyses for rat carotid balloon injury model," Methods Mol. Med. **139**, 31–66 (2007).
41. N. G. Horton and C. Xu, "Dispersion compensation in three-photon fluorescence microscopy at 1,700 nm," Biomed. Opt. Express **6**(4), 1392–1397 (2015).
42. Š. Lhoták, G. Gyulay, J. C. Cutz, A. Al-Hashimi, B. L. Trigatti, C. D. Richards, S. A. Igdoura, G. R. Steinberg, J. Bramson, K. Ask, and R. C. Austin, "Characterization of proliferating lesion-resident cells during all stages of atherosclerotic growth," J. Am. Heart Assoc. **5**(8), e003945 (2016).
43. H. C. Stary, A. B. Chandler, R. E. Dinsmore, V. Fuster, S. Glagov, W. Insull, Jr., M. E. Rosenfeld, C. J. Schwartz, W. D. Wagner, and R. W. Wissler, "A definition of advanced types of atherosclerotic lesions and a histological classification of atherosclerosis. A report from the Committee on Vascular Lesions of the Council on Arteriosclerosis, American Heart Association," Arterioscler. Thromb. Vasc. Biol. **15**(9), 1512–1531 (1995).
44. R. Virmani, F. D. Kolodgie, A. P. Burke, A. Farb, and S. M. Schwartz, "Lessons from sudden coronary death: a comprehensive morphological classification scheme for atherosclerotic lesions," Arterioscler. Thromb. Vasc. Biol. **20**(5), 1262–1275 (2000).
45. Y. Nakashima, H. Fujii, S. Sumiyoshi, T. N. Wight, and K. Sueishi, "Early human atherosclerosis: accumulation of lipid and proteoglycans in intimal thickenings followed by macrophage infiltration," Arterioscler. Thromb. Vasc. Biol. **27**(5), 1159–1165 (2007).
46. A. J. Lusis, "Atherosclerosis," Nature **407**(6801), 233–241 (2000).
47. J. L. Suhalim, C. Y. Chung, M. B. Lilledahl, R. S. Lim, M. Levi, B. J. Tromberg, and E. O. Potma, "Characterization of cholesterol crystals in atherosclerotic plaques using stimulated Raman scattering and second-harmonic generation microscopy," Biophys. J. **102**(8), 1988–1995 (2012).
48. H. N. Hutson, T. Marohl, M. Anderson, K. Eliceiri, P. Campagnola, and K. S. Masters, "Calcific aortic valve disease is associated with layer-specific alterations in collagen architecture," PLoS One **11**(9), e0163858 (2016).
49. L. M. Zadrozny, E. B. Neufeld, B. M. Lucotte, P. S. Connelly, Z. X. Yu, L. Dao, L. Y. Hsu, and R. S. Balaban, "Study of the development of the mouse thoracic aorta three-dimensional macromolecular structure using two-photon microscopy," J. Histochem. Cytochem. **63**(1), 8–21 (2015).
50. W. Yu, J. C. Braz, A. M. Dutton, P. Prusakov, and M. Rekhter, "In vivo imaging of atherosclerotic plaques in apolipoprotein E deficient mice using nonlinear microscopy," J. Biomed. Opt. **12**(5), 054008 (2007).
51. A. Zoumi, X. Lu, G. S. Kassab, and B. J. Tromberg, "Imaging coronary artery microstructure using second-harmonic and two-photon fluorescence microscopy," Biophys. J. **87**(4), 2778–2786 (2004).
52. R. S. Lim, A. Kratzer, N. P. Barry, S. Miyazaki-Anzai, M. Miyazaki, W. W. Mantulin, M. Levi, E. O. Potma, and B. J. Tromberg, "Multimodal CARS microscopy determination of the impact of diet on macrophage infiltration and lipid accumulation on plaque formation in ApoE-deficient mice," J. Lipid Res. **51**(7), 1729–1737 (2010).
53. R. Chèvre, J. M. González-Granado, R. T. Megens, V. Sreeramkumar, C. Silvestre-Roig, P. Molina-Sánchez, C. Weber, O. Soehnlein, A. Hidalgo, and V. Andrés, "High-resolution imaging of intravascular atherogenic inflammation in live mice," Circ. Res. **114**(5), 770–779 (2014).
54. Z. Wu, A. Curaj, S. Fokong, E. A. Liehn, C. Weber, T. Lammers, F. Kiessling, and M. Zandvoort van, "Rhodamine-loaded intercellular adhesion molecule-1-targeted microbubbles for dual-modality imaging under controlled shear stresses," Circ Cardiovasc Imaging **6**(6), 974–981 (2013).
55. K. Arakawa, K. Isoda, T. Ito, K. Nakajima, T. Shibuya, and F. Ohsuzu, "Fluorescence analysis of biochemical constituents identifies atherosclerotic plaque with a thin fibrous cap," Arterioscler. Thromb. Vasc. Biol. **22**(6), 1002–1007 (2002).
56. G. van Soest, E. Regar, T. P. Goderie, N. Gonzalo, S. Koljenović, G. J. van Leenders, P. W. Serruys, and A. F. van der Steen, "Pitfalls in plaque characterization by OCT: image artifacts in native coronary arteries," JACC Cardiovasc. Imaging **4**(7), 810–813 (2011).
57. G. J. Ughi, H. Wang, E. Gerbaud, J. A. Gardecki, A. M. Fard, E. Hamidi, P. Vacas-Jacques, M. Rosenberg, F. A. Jaffer, and G. J. Tearney, "Clinical characterization of coronary atherosclerosis with dual-modality OCT and near-infrared autofluorescence imaging," JACC Cardiovasc. Imaging **9**(11), 1304–1314 (2016).

Biomedical Optics EXPRESS

58. T. Wang, A. McElroy, D. Halaney, D. Vela, E. Fung, S. Hossain, J. Phipps, B. Wang, B. Yin, M. D. Feldman, and T. E. Milner, "Dual-modality fiber-based OCT-TPL imaging system for simultaneous microstructural and molecular analysis of atherosclerotic plaques," Biomed. Opt. Express **6**(5), 1665–1678 (2015).
59. R. Turcotte, D. J. Rutledge, E. Bélanger, D. Dill, W. B. Macklin, and D. C. Côté, "Intravital assessment of myelin molecular order with polarimetric multiphoton microscopy," Sci. Rep. **6**(1), 31685 (2016).
60. H. W. Wang, I. M. Langohr, M. Sturek, and J. X. Cheng, "Imaging and quantitative analysis of atherosclerotic lesions by CARS-based multimodal nonlinear optical microscopy," Arterioscler. Thromb. Vasc. Biol. **29**(9), 1342–1348 (2009).
61. A. Zumbusch, G. R. Holtom, and X. S. Xie, "Three-dimensional vibrational imaging by coherent anti-Stokes Raman scattering," Phys. Rev. Lett. **82**(20), 4142–4145 (1999).
62. J. X. Cheng and X. S. Xie, "Coherent Anti-Stokes Raman Scattering Microscopy: Instrumentation, Theory, and Applications," J. Phys. Chem. B **108**(3), 827–840 (2004).
63. L. Marcu, J. A. Jo, Q. Fang, T. Papaioannou, T. Reil, J. H. Qiao, J. D. Baker, J. A. Freischlag, and M. C. Fishbein, "Detection of rupture-prone atherosclerotic plaques by time-resolved laser-induced fluorescence spectroscopy," Atherosclerosis **204**(1), 156–164 (2009).
64. J. A. Jo, Q. Fang, T. Papaioannou, J. D. Baker, A. H. Dorafshar, T. Reil, J. H. Qiao, M. C. Fishbein, J. A. Freischlag, and L. Marcu, "Laguerre-based method for analysis of time-resolved fluorescence data: application to in-vivo characterization and diagnosis of atherosclerotic lesions," J. Biomed. Opt. **11**(2), 021004 (2006).
65. S. Dochow, H. Fatakdawala, J. E. Phipps, D. Ma, T. Bocklitz, M. Schmitt, J. W. Bishop, K. B. Margulies, L. Marcu, and J. Popp, "Comparing Raman and fluorescence lifetime spectroscopy from human atherosclerotic lesions using a bimodal probe," J. Biophotonics **9**(9), 958–966 (2016).
66. J. A. Jo, J. Park, P. Pande, S. Shrestha, M. J. Serafino, J. J. Rico Jimenez, F. Clubb, B. Walton, L. M. Buja, J. E. Phipps, M. D. Feldman, J. Adame, and B. E. Applegate, "Simultaneous morphological and biochemical endogenous optical imaging of atherosclerosis," Eur. Heart J. Cardiovasc. Imaging **16**(8), 910–918 (2015).
67. H. Fatakdawala, D. Gorpas, J. W. Bishop, J. Bec, D. Ma, J. A. Southard, K. B. Margulies, and L. Marcu, "Fluorescence lifetime imaging combined with conventional intravascular ultrasound for enhanced assessment of atherosclerotic plaques: an ex vivo study in human coronary arteries," J. Cardiovasc. Transl. Res. **8**(4), 253–263 (2015).
68. T. Wang, D. Halaney, D. Ho, M. D. Feldman, and T. E. Milner, "Two-photon luminescence properties of gold nanorods," Biomed. Opt. Express **4**(4), 584–595 (2013).
69. T. Wang, A. McElroy, D. Halaney, D. Vela, E. Fung, S. Hossain, J. Phipps, B. Wang, B. Yin, M. D. Feldman, and T. E. Milner, "Detection of plaque structure and composition using OCT combined with two-photon luminescence (TPL) imaging," Lasers Surg. Med. **47**(6), 485–494 (2015).
70. T. Wang, J. J. Mancuso, S. M. Kazmi, J. Dwelle, V. Sapozhnikova, B. Willsey, L. L. Ma, J. Qiu, X. Li, A. K. Dunn, K. P. Johnston, M. D. Feldman, and T. E. Milner, "Combined two-photon luminescence microscopy and OCT for macrophage detection in the hypercholesterolemic rabbit aorta using plasmonic gold nanorose," Lasers Surg. Med. **44**(1), 49–59 (2012).
71. T. T. Le, I. M. Langohr, M. J. Locker, M. Sturek, and J. X. Cheng, "Label-free molecular imaging of atherosclerotic lesions using multimodal nonlinear optical microscopy," J. Biomed. Opt. **12**(5), 054007 (2007).
72. T. Meyer, M. Chemnitz, M. Baumgartl, T. Gottschall, T. Pascher, C. Matthäus, B. F. Romeike, B. R. Brehm, J. Limpert, A. Tünnermann, M. Schmitt, B. Dietzek, and J. Popp, "Expanding multimodal microscopy by high spectral resolution coherent anti-Stokes Raman scattering imaging for clinical disease diagnostics," Anal. Chem. **85**(14), 6703–6715 (2013).
73. E. V. Gubarkova, V. V. Dudenkova, F. I. Feldchtein, L. B. Timofeeva, E. B. Kiseleva, S. S. Kuznetsov, B. E. Shakhov, A. A. Moiseev, V. M. Gelikonov, G. V. Gelikonov, A. Vitkin, and N. D. Gladkova, "Multi-modal optical imaging characterization of atherosclerotic plaques," J. Biophotonics **9**(10), 1009–1020 (2016).
74. N. G. Horton, K. Wang, D. Kobat, C. G. Clark, F. W. Wise, C. B. Schaffer, and C. Xu, "In vivo three-photon microscopy of subcortical structures within an intact mouse brain," Nat. Photonics **7**(3), 205–209 (2013).
75. D. Kobat, N. G. Horton, and C. Xu, "In vivo two-photon microscopy to 1.6-mm depth in mouse cortex," J. Biomed. Opt. **16**(10), 106014 (2011).
76. C. Xu and F. W. Wise, "Recent Advances in Fiber Lasers for Nonlinear Microscopy," Nat. Photonics **7**(12), 1006 (2013).
77. D. Sinefeld, H. P. Paudel, D. G. Ouzounov, T. G. Bifano, and C. Xu, "Adaptive optics in multiphoton microscopy: comparison of two, three and four photon fluorescence," Opt. Express **23**(24), 31472–31483 (2015).
78. N. Ji, "Adaptive optical fluorescence microscopy," Nat. Methods **14**(4), 374–380 (2017).
79. S. H. Chia, C. H. Yu, C. H. Lin, N. C. Cheng, T. M. Liu, M. C. Chan, I. H. Chen, and C. K. Sun, "Miniaturized video-rate epi-third-harmonic-generation fiber-microscope," Opt. Express **18**(16), 17382–17391 (2010).
80. C. L. Hoy, O. Ferhanoğlu, M. Yildirim, W. Piyawattanametha, H. Ra, O. Solgaard, and A. Ben-Yakar, "Optical design and imaging performance testing of a 9.6-mm diameter femtosecond laser microsurgery probe," Opt. Express **19**(11), 10536–10552 (2011).
81. D. M. Huland, K. Charan, D. G. Ouzounov, J. S. Jones, N. Nishimura, and C. Xu, "Three-photon excited fluorescence imaging of unstained tissue using a GRIN lens endoscope," Biomed. Opt. Express **4**(5), 652–658 (2013).

Biomedical Optics EXPRESS

82. C. M. Brown, D. R. Rivera, I. Pavlova, D. G. Ouzounov, W. O. Williams, S. Mohanan, W. W. Webb, and C. Xu, "In vivo imaging of unstained tissues using a compact and flexible multiphoton microendoscope," J. Biomed. Opt. **17**(4), 040505 (2012).

1. Introduction

Atherosclerosis is characterized by the thickening and gradual accumulation of fat within the artery wall [1,2] and is a major cause of heart and cerebrovascular diseases worldwide [3,4]. Therefore, a greater understanding of the cellular mechanisms responsible for this condition, as well as less invasive and more sensitive technologies to monitor plaque formation in vivo, are needed.

Current clinical techniques used to evaluate atherosclerosis include x-ray angiography [5–7], magnetic resonance imaging [8–10], intravascular ultrasound (IVUS) [11–13], and optical coherence tomography (OCT) [14–16]. Although these imaging strategies provide clinical information such as vessel morphology and, in some cases, thickness of the vessel wall, they are limited in their capacity to provide cell-scale resolution. For example, angiography, which shows the vessel lumen shape using an injected contrast agent, often fails to detect early wall composition changes that do not obstruct the lumen [17]. OCT and IVUS are able to detect changes within the vessel wall, but spatial resolutions are not quite sufficient to detect sub-cellular alterations during early plaque formation (axial resolutions of 150 – 200 μm and 10 – 18 μm for IVUS and OCT, respectively [13, 14]). OCT and third harmonic generation (THG) signals both depend on index of refraction changes at interfaces. THG also depends on the $\chi^{(3)}(3\omega;\omega,\omega,\omega)$ tensor, suggesting an additional mechanism based on chemical composition for contrast with THG [18].

The scientific understanding of atherosclerosis has primarily relied on histopathology and electron microscopy of post-mortem tissue [14,19–22]. Although high resolution and chemically specific, these techniques involve extensive tissue processing and cumbersome histological sectioning that may alter the structure and biochemical properties of the tissue. Multiphoton microscopy has emerged as an ideal imaging modality that is sensitive to specific molecules and structures in biological tissues [23–25] and can be used in vivo [26–31].

THG is an endogenous contrast mechanism, which facilitates in vivo experiments and opens up the possibility for clinical use. THG occurs when three photons at the excitation laser frequency are converted to one photon at three times the excitation frequency [32,33]. THG has been used in conjunction with two-photon excited fluorescence (2PEF) to image cellular lipid droplets [34], and myelin, a dense lipid sheath around axons, in the mouse brain and spinal cord [35]. It has been previously demonstrated that pure free fatty acid samples generate THG [36]. Seeger and colleagues have shown THG detection in a cross-sectional view of a histological section of atherosclerosis, but a better understanding of the signal source is needed [37]. We hypothesized that lipid structures in atherosclerotic plaques are an ideal target for THG imaging. Such imaging would be impactful in many applications due to the high prevalence and clinical significance of lipid bodies [1,38].

In this work, we demonstrate imaging of atherosclerotic lesions using label-free multiphoton microscopy with excitation in the MIR range. Using a genetic knockout mouse model of atherosclerosis and diseased human coronary artery samples, we show the ability to produce detailed, three-dimensional and high resolution optical sections of atherosclerotic plaques. In addition to THG microscopy of lipid bodies, simultaneous SHG and autofluorescence show anatomical structures within label-free images. This technology is an important addition to the microscopy tool kit for studies of atherosclerosis.

Biomedical Optics EXPRESS

2. Materials and methods

2.1 Mouse model of atherosclerosis

Test samples were harvested from mice lacking the apolipoprotein E gene ($ApoE^{-/-}$) which develop hypercholesterolemia and spontaneous atherosclerosis that closely mimics the human disease [39]. 2 – 4-month-old male and female $ApoE^{-/-}$ mice (n = 4) (Jackson Labs Stock #002052) were fed a high fat diet (HFD) for 16-weeks (Harlan TD.88137: protein 17.3%; carbohydrate 48.5%; fat 21.2% by weight). C57BL/6, age-matched, wild type (WT) mice (n = 3) fed a normal chow diet were used as controls. All animal care and experimental procedures were approved by the Institutional Animal Care and Use Committee of Cornell University and comply with the Guide for the Care and Use of Laboratory Animals by the National Institutes of Health.

2.2 Preparation of mouse aorta for imaging

To collect aortas, free-breathing mice were anesthetized with a mixture of 3% isoflurane gas in oxygen. A thoracotomy was performed, the right atrium punctured, and blood removed from the heart and aorta by perfusion of cold phosphate buffered saline (PBS) through the left ventricle until the perfusate was clear. This was followed by perfusion of cold 4% paraformaldehyde (PFA) in PBS. The heart and attached aorta (arch, thoracic and abdominal segments) were dissected and immersed in 4% PFA in PBS overnight, followed by 30% sucrose in PBS at 4°C. For whole mount imaging, the aortic arch was micro-dissected from the heart and thoracic aorta, then split lengthwise to expose the luminal surface. The aorta was placed on a glass slide, immersed in PBS with the luminal surface facing upwards and covered with a coverglass. For cryosections, aortas were frozen in Optimal Cutting Temperature compound (Tissue-Tek, Sakura Finetek Inc.) and sectioned in a cryo-microtome with 7-μm or 20-μm thickness.

2.3 Preparation of human coronary artery for imaging

Human coronary arteries were provided by Anabios Corporation. All human tissues used for this study were obtained in the U.S.A. from organ donors following legal consent. Tissues were collected from one normal and one atherosclerotic heart. Tissues were derived from brain dead donors and the hearts removed at the same time as transplantable organs within an hour post cross-clamp. At the time of harvest, the human hearts were perfused with an ice-cold proprietary cardioplegic solution. Upon arriving in the laboratory, the heart was re-perfused with a proprietary recovery solution. Subsequently, sections of the coronary arteries were dissected using micro-scissors and tweezers, immediately fixed in 10% buffered formalin and then transferred to 70% ethanol after 24 hours and stored at 4° C. Approximately 12 months had passed from when the tissue had been placed in 70% ethanol. Prior to imaging, samples were immersed in 30% sucrose in PBS at 4° C for 1 week. Approximately 1-cm long sections of arteries were dissected from the provided sample, and macroscopic areas of plaque deposition were identified under a stereoscope. Sections of artery were further dissected around regions of plaque to obtain a flat sample. A coverglass was placed on the luminal surface and held in place with tape. PBS was added underneath the coverslip to prevent the sample from drying during imaging. After multiphoton imaging, samples were frozen and sectioned for histology.

2.4 Histology and immunofluorescence

Serial cross-sections of human and mouse aortas were stained with hematoxylin and eosin (H&E) and Masson's Trichrome for collagen using standard procedures [40]. For Nile-Red staining of lipids, 20-μm sections of aortas from $ApoE^{-/-}$-HFD were immersed in 5 μg/mL Nile-Red diluted in PBS for 30 min at room temperature. Sections were washed thoroughly in PBS and then coverslipped in PBS. CD68 immunofluorescence was performed on 7-μm

Biomedical Optics EXPRESS

human coronary artery sections to identify regional macrophage and foam cell location and its relationship to THG signal. Sections were incubated in 1% sodium dodecyl sulfate in PBS for 5 min. To block non-specific binding, blocking buffer (3% bovine serum albumin, 10% goat serum, 0.1% Triton X-100 in PBS) was added for 30 min. Sections were then incubated with CD68 primary antibody (1:50, sc-20060; Santa Cruz Biotechnology Inc.) diluted in blocking buffer overnight at 4°C. Following three washes in PBS, goat anti-mouse Alexa-Fluor 594 secondary antibody (1:200, A11005; Thermo Scientific) was applied diluted in PBS for 30 min at room temperature. Slides were then washed, and mounted with aqueous mounting medium containing DAPI for cell nuclei (Vectashield, H-1200; Vector Laboratories). Confocal microscopy was performed on a Zeiss LSM880 Confocal inverted microscope using a Zeiss plan apochromatic 40x 1.4 NA oil objective controlled by ZEN 2.1 SPC software. Laser lines for DAPI and Alexa-594 were 405 nm and 561 nm respectively, and signal was collected between 410 and 496 nm (DAPI) and 588–733 nm (Alexa-594).

2.5 Multiphoton microscopy

Imaging was conducted using a custom multiphoton microscope equipped with four epi-detection backward scattered channels, the option of two MIR sources used for harmonic generation, as well as a Ti:Sapphire oscillator (Chameleon, Coherent) for 2PEF. 1,700-nm laser light (~100-fs pulse length, 40-nm full-width-half-max (FWHM) bandwidth) was produced through a soliton self-frequency shift of 1,550-nm femtosecond pulses from a commercial fiber laser (FLCPA-02CCNU15, Calmar Lasers) through a photonic crystal rod with a fundamental mode area of 3500 μm^2 (NC420-152-EE45, NKT Photonics). For 1,700-nm lasers, dispersion is compensated using stacked silicon wafers (University Wafer ID# 2808) set at Brewster's angle [41]. To generate 1,300 nm laser light, an optical parametric amplifier (OPA) (Coherent, Opera-F) was seeded by a diode-pumped femtosecond laser (60 µJ/pulse at 1 MHz; Coherent, Monaco). Dispersion for 1,300-nm excitation was compensated with an SF10 prism pair [27]. For imaging, the excitation laser was scanned with a line rate of ~1kHz with galvanometric scanners. Images were acquired with an Olympus XLPlan N 25x 1.05 NA objective customized for MIR excitation wavelengths. Images of 0.175 ± 0.005 µm diameter microspheres (PS-Speck Microscope Point Source Kit P7220) had intensities profiles with the full-width half max of 3.39 µm axial and 0.85 µm lateral with 1,300 nm, and 2.64 µm lateral and 2.02 µm axial with 1,700 nm. When imaging with 1,700 nm, heavy water (D_2O) was used for index matching between the coverglass and the objective in order to minimize absorption of the excitation light [41]. For two-photon excited fluorescence (2PEF) microscopy of Nile-Red, images were acquired using a Ti:Sapphire laser with the wavelength centered at 810 nm using an off-the-shelf Olympus XLPlan N 25x 1.05 NA objective. Signal was collected using custom detections optics using a primary dichroic suited for either MIR or NIR (near-infrared) laser transmission (BLP01-980R-49x70, FF705-Di01-49x70, Semrock), secondary dichroic (FF01-593/LP-90x108, Semrock), two tertiary dichroic (FF801-Di02-90x108, Di02-R488-90x108, Semrock), and bandpass filters on each detection channel (FF01-433/24-25, Semrock, FF01-560/25-25, Semrock, NC528423 – ET645/65m, Chroma, and FF01-834/LP-25, Semrock). For each $ApoE^{-/-}$ mouse or human coronary artery sample, 3 – 6 z-stacks were taken within different regions of the same sample. 512 x 512 pixel frames were acquired at 1.8 frames/sec (dwell time of 2 µs/pixel). Therefore a 0.067 cm^3 volume took approximately two minutes to complete. All images were processed using ImageJ (National Institutes of Health). Projections were maximum intensity projections over thicknesses noted in the caption. Images for display were background subtracted (rolling ball radius, 50 pixels) and a median filter (2 pixels) was applied. Contrast was adjusted for each image manually by adjusting the maximum and minimum displayed values while maintaining a linear intensity relationship within the displayed range.

Biomedical Optics EXPRESS

3. Results

3.1 THG of atherosclerotic plaques

We imaged whole-mounted aortas, illuminated from either the luminal or abluminal side of the tissue, from a mouse model of atherosclerosis fed a high-fat diet for 16 weeks in regions where plaques were visible by eye and similar regions from wild type mice fed normal diets as control. All ApoE$^{-/-}$ (4 mice) samples contained atherosclerotic plaques and no WT samples (3 mice) contained atherosclerosis. Only atherosclerotic regions in ApoE$^{-/-}$ mice were imaged. Using multiphoton microscopy excited with 1,700 nm excitation (1 MHz, less than 35 mW at surface) several nonlinear optical processes provide contrast that distinguish morphological features throughout the healthy and diseased vessel wall. In both atherosclerotic and control samples, SHG, detected at 802-835 nm, was present at the outer adventitial surface and was spatially and morphologically consistent with collagen fibers (Fig. 1(a) and 1(c)). A striated pattern with the broad spectral emission of elastin autofluorescence was visible within the vessel walls at 613–678 nm and within the THG range (548–573 nm) (Fig. 1(c-ii)). Aortas from ApoE$^{-/-}$-HFD mice had distinct, bright, globular structures in the THG spectral emission range of 548-573 nm near the luminal surface (Fig. 1(a-i)) and deeper within the vessel wall at levels with the elastin autofluorescence (Fig. 1(a-ii)). Comparison to histological sections of the same treatment group (Masson's Trichrome and H&E staining, Fig. 1(b)) revealed lipid deposits within the tunica intima that appear similar in morphology to deposits in multiphoton microscopy cross-sectional views. Such structures were not present in WT-Normal aortas (Fig. 1(c) and 1(d)).

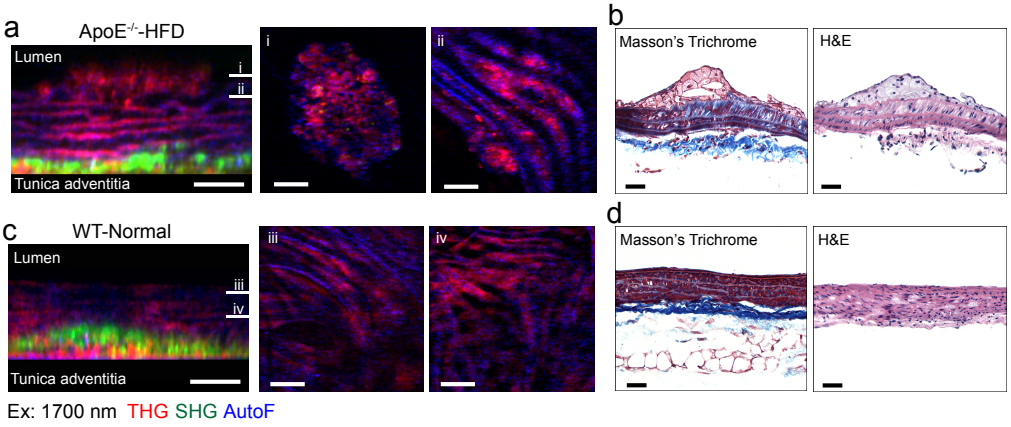

Fig. 1. Multiphoton microscopy shows vessel wall structures consistent with atherosclerotic lesions in whole-mounted aortas extracted from a murine model of atherosclerosis. (a) Aorta from an apolipoprotein E knockout mouse fed a high fat diet (ApoE$^{-/-}$-HFD) shown with cross-sectional and enface views (i and ii) through a region with strong emission at the third harmonic generation (THG) wavelengths. Laser excitation was at 1,700 nm, incident on the lumen. (b) Histology with Masson's trichrome and H&E staining of aorta from an ApoE$^{-/-}$-HFD mouse. (c) Aorta from a wild type mice fed a normal chow diet (WT-Normal) and cross-sectional and enface views (iii and iv). (d) Histology of aorta from a WT-Normal mouse. Cross-sectional views in a and c are maximum intensity projections through the y-axis. Second harmonic generation (SHG); autofluorescence (AutoF). Scale bars are 50 μm.

To confirm that the source of THG is from lipids, Nile-Red was used to stain lipids in ApoE$^{-/-}$-HFD tissue sections (3 ROI from 2 mice). Imaging of the same region of interest using 2PEF for Nile-Red (Fig. 2(a): Ex: 810 nm; Em: 612–677 nm) and 1,700 nm excitation light for THG (Em: 535–585 nm), demonstrated that the structures with strong THG signal also have strong Nile-Red signal (Fig. 2(b)), suggesting that the source of THG is the lipids within atherosclerotic plaques.

Biomedical Optics EXPRESS

Multiphoton microscopy using 1,300 nm excitation showed similar structures as 1,700 nm excitation in the vessel wall and at the luminal surface in the THG spectral range of 421–445 nm (Fig. 3(a) and 3(b)). Unlike fluorescence, the wavelength of THG depends on the excitation wavelength. Therefore, to identify the features giving rise to THG, 1,300-nm and 1,700-nm excitation were used to image the same ApoE$^{-/-}$-HFD sample at a region that had atherosclerotic features. Emission channels that included the THG wavelengths, 421–445 nm for 1,300 nm and 548–573 nm for 1,700 nm, generated similar images, while the alternate channels showed little signal (Fig. 3(c) and 3(d)). This change in emission wavelengths is consistent with THG.

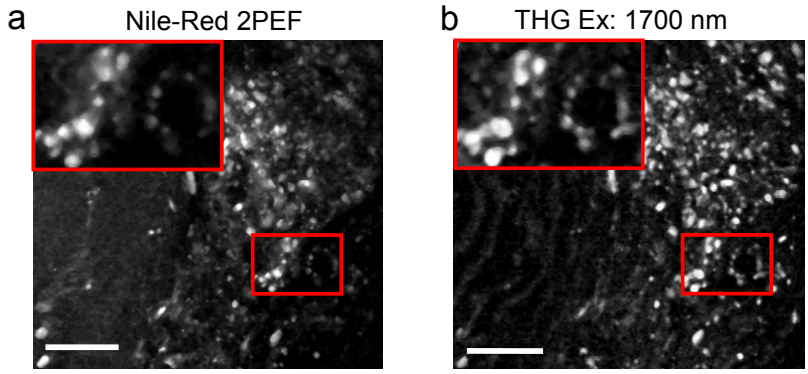

Fig. 2. Correlation between third harmonic generation (THG) and lipid stain. (a) Frozen section (20-µm thickness) of aorta from ApoE$^{-/-}$-HFD stained for lipids using Nile-Red and imaged using two-photon excited fluorescence (2PEF) at 810 nm excitation. Displayed image shows fluorescence channel for Nile-Red (612–677 nm). (b) Same section imaged with 1,700 nm excitation showing the THG channel detected with 548–573 nm band pass filter. Scale bars are 50 µm.

WT-Normal aortas generally appeared similar, even between different mice (Fig. 4(a) and Fig. 1(c)). Consistent structures included the medial layer that primarily consists of smooth muscle cells and elastin that generated autofluorescence and a weak THG signal (Fig. 4(a-ii)). Collagen of the tunica adventitia produced SHG in both normal and atherosclerotic samples (Fig. 4(a-iii) and 4(b-iii)). THG on the abluminal side of the vessel was due to adventitial fat that was sometime present following aorta dissection (Fig. 4(b)) and was closely associated with SHG in the adventitial layer.

Biomedical Optics EXPRESS

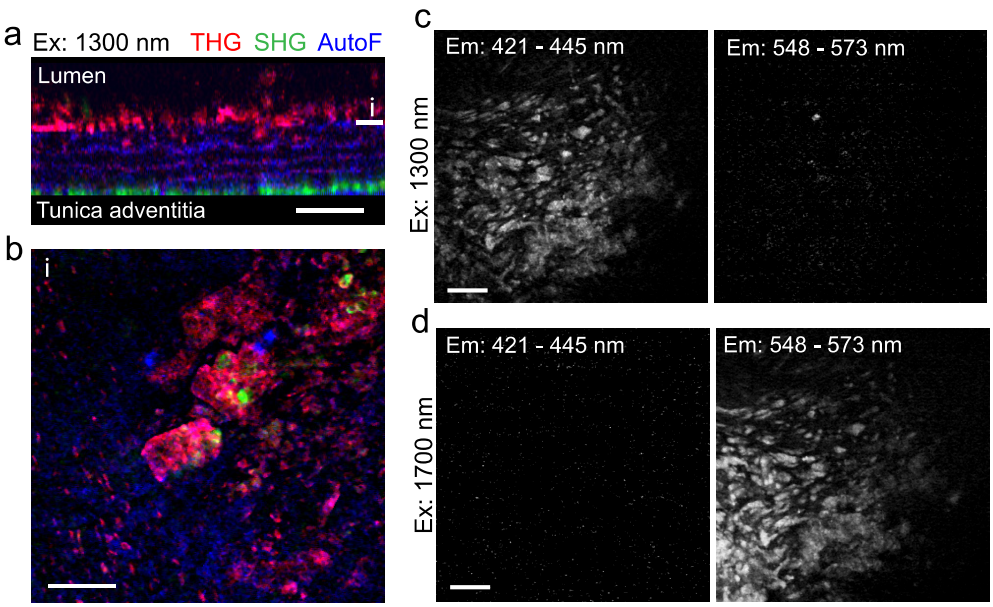

Fig. 3. Optical properties of atherosclerotic lesions in mouse aorta. (a and b) 1,300 nm excitation produces signals at third harmonic generation (THG) and second harmonic generation (SHG) wavelengths as well as autofluorescence (AutoF) at an atherosclerotic lesion. Cross-sectional, maximum projected (a) and enface (b) views of ApoE$^{-/-}$-HFD aorta. Line in a shows location of b. (c) 1,300 nm excitation of a region within ApoE$^{-/-}$-HFD aorta that has atherosclerotic features, produces a strong signal in the THG emission range (421–445 nm). (d) 1,700 nm excitation of the same region shows the same features in the THG emission range (548–573 nm). Scale bars are 50 µm.

ApoE$^{-/-}$-HFD arteries displayed highly variable morphologies and features even within the same mouse. In an example of pathology that extended across a wide area, THG appeared in scattered, smaller patches throughout the luminal half of the vessel wall (Fig. 4(b)). THG clearly identified an area of intimal thickening of ApoE$^{-/-}$-HFD vessel wall by the presence of punctate regions indicating lipids (Fig. 4(b-i)) that are not present in WT-Normal (Fig. 4(a-i)). Different samples revealed a variety of plaque features that could be detected with THG imaging (Fig. 4(c)-4(f)). Furthermore, different sizes and structures of plaque development can be observed between the same sample within different regions. THG signals varied from continuous large deposits near the lumen (Fig. 4(c)) to punctate regions of lipid deposits about 8 µm in size within deeper layers of the intima (Fig. 4(d) and 4(e)). Images from a region of vessel bifurcation from the aortic arch (Fig. 4(f)), revealed similar structures and signals within the tissue - THG at the luminal surface, then elastin and collagens revealed by autofluorescence and SHG towards the abluminal surface, respectively. Occasionally, SHG was detected in close association within larger THG regions of plaques (Fig. 4, arrows). Figure 4(f) also shows the detection of SHG (collagen) within the medial layer in close association with autofluorescence. Both 1,300 nm and 1,700 nm excitation sources were able to image through the entire vessel wall of ApoE$^{-/-}$ and WT mice (70 – 150 µm).

Biomedical Optics EXPRESS

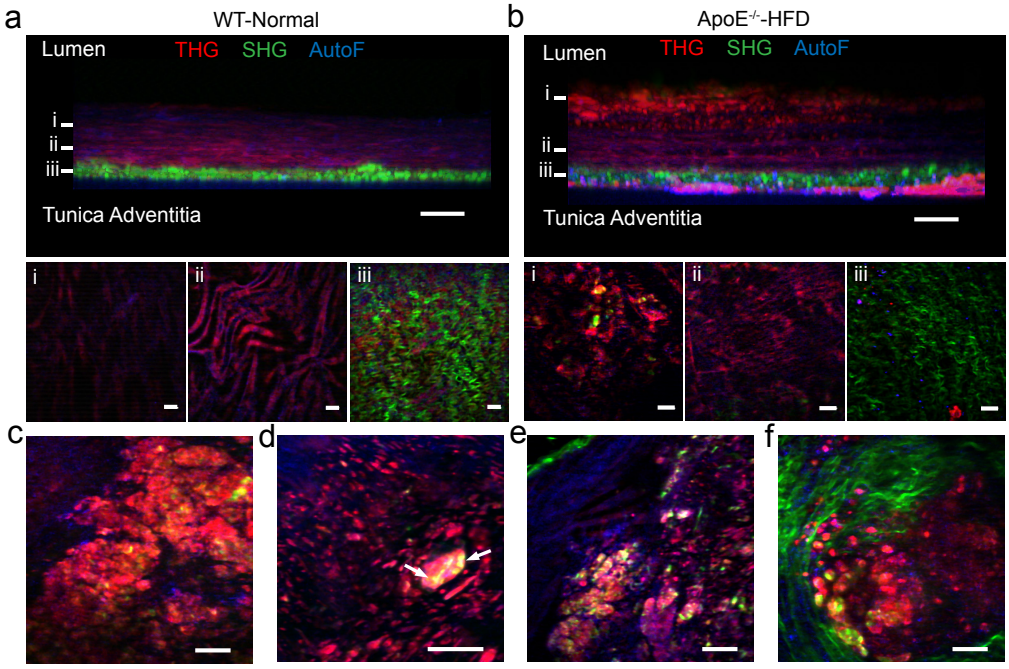

Fig. 4. Third harmonic generation (THG) microscopy using 1,700 nm excitation reveals varying features of atherosclerotic lesions. (a) WT-Normal and (b) ApoE$^{-/-}$-HFD mouse aortas shown in cross-sectional projections and enface views, show second harmonic generation (SHG) of the tunica adventitia (a-iii and b-iii), autofluorescence (AutoF) in the media (a-ii and b-ii) and a strong THG signal within the thickened intimal layer of ApoE$^{-/-}$-HFD (b-i) that is not present in WT-Normal (a-i). Single z-slices through different lesions (c-f) show variability in structures producing THG signal and the association between SHG, THG and AutoF. (c) Large deposit of THG signal 38 µm below lumen. (d) Small punctate regions of THG signal 48 µm below lumen, with SHG positioned in close association with THG (arrows). (e) Image from near the abluminal edge of aorta showing THG and SHG deposits. (f) Plaque near a vessel bifurcation off of the aortic arch. Scale bars are 50 µm.

3.2 Human coronary artery THG imaging

We used THG microscopy (1,300 nm) to demonstrate the capability to image atherosclerosis within a human coronary artery (Fig. 5). Two different human coronary artery samples were imaged with THG microscopy, a healthy coronary artery (Fig. 5(a)) and a coronary artery that had been classified as coronary artery disease and had macroscopically visible plaques (Fig. 5(b)). When mounted with the lumen side towards the objective, we were able to image through the entire 270-µm thickness of the healthy coronary artery wall from the intima to the adventitia. Intrinsic contrast mechanisms showed characteristic features of the vessel wall similar to mouse aorta. This included SHG of collagen fibers within the adventitia, and autofluorescence from elastin that was particularly evident within the internal elastin lamina (Fig. 5(a-ii)).

Biomedical Optics EXPRESS

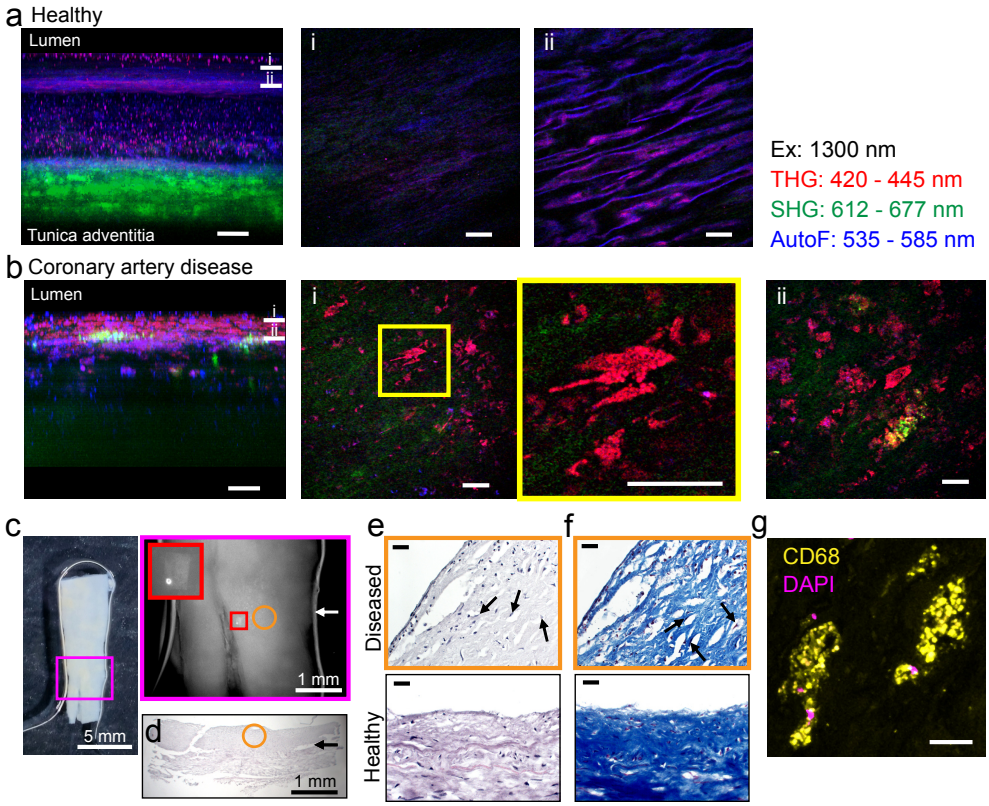

Fig. 5. Third harmonic generation (THG) microscopy of human coronary artery. (a) In a healthy coronary artery imaged from the luminal side with 1,300 nm excitation, a cross-sectional projection and enface planes (i and ii) show second harmonic generation (SHG) and broad autofluorescence (AutoF) throughout the intimal layer. (b) An artery sample with coronary artery disease imaged from the luminal side with 1,300 nm. i and ii show images from levels indicated in cross-sectional view. Yellow box shows location of magnified view. (c) Photograph and epi-fluorescence image of sample imaged in (b). Magenta box shows the locations of magnified regions. A small laser burn (red box) was induced during THG microscopy at a measured displacement to the imaged region in (b) indicated with an orange circle to aid in image registration. A 23-gauge needle was used to make a fiduciary mark (arrows). (d) Bright-field image of region imaged with multiphoton microscopy from a section of the tissue with fiduciary mark (black arrow). (e) Higher magnification images from the region imaged with multiphoton microscopy stained with H&E and (f) Masson's Trichrome. Open, nucleated spaces (arrows) are consistent with lipid deposits. Sections from a sample with no atherosclerosis (healthy) are shown below. (g) Confocal microscopy of immunostaining for CD68 in a section from the same region. Unless otherwise noted, scale bars are 50 µm.

In the coronary artery disease sample, the imaging depth when imaged from the lumen was limited to the intima and media layers and reached 400 µm in depth. Like in the mouse aorta, THG appeared in distinct patches within intimal layers. Some THG patches showed granular structures (~3-µm nodules) with THG signal suggesting a sub-cellular source (Fig. 4(b-i) and 4(b-ii)). Throughout intimal and medial layers, weak, diffuse SHG and autofluorescent signal were present in regions around THG-emitting deposits. In some locations in the intima, SHG appeared in clusters of bright, 30 – 70 µm spots (Fig. 5(b-ii)). To confirm the presences of atherosclerotic lesions in this tissue, we sectioned and stained the sample. For registration of the multiphoton microscopy images to histological sections, a small laser burn was induced at a measured displacement from the imaged region during THG imaging (Fig. 5(c)). Wide-field fluorescence microscopy of the intrinsic autofluorescence was

Biomedical Optics EXPRESS

used to find the marked region. With this image for positioning, a 23-gauge needle was inserted into the side of the tissue as a fiducial to identify sections taken through the imaged region for histological processing (Fig. 5(d)). H&E staining revealed clear spaces within the imaged region, characteristic of macrophage foam cells that previously contained lipids in vivo and are marked by a remaining nucleus (Fig. 5(e)) [42]. Masson's Trichrome staining revealed similar structures and collagen throughout the lesion (Fig. 5(f)). Healthy control tissue did not show these features. Immunofluorescence confirmed the presence of CD68-positive macrophage foam cells within the imaged region that showed similarly-shaped, THG-positive structures (Fig. 5(g)). H&E, Masson's Trichrome and CD68 immunofluorescence was performed on two additional histological sections and the same result was observed (data not shown).

4. Discussion

Despite significant advances in the understanding and clinical monitoring of vessel wall pathology in coronary artery disease, atherosclerosis remains a major health problem. We have demonstrated that a strong THG signal is generated from atherosclerotic plaques in both rodent and human artery samples. Used in conjunction with other nonlinear optical processes such as SHG and autofluorescence, this technique could be used to characterize atherosclerotic lesions in label-free tissue.

We observed a range of structures with THG signal in diseased vessels that resemble features found in standard histological classification of atherosclerotic plaques [2,43,44] (Fig. 6). The THG-producing structures that we observed are similar in morphology to lipid-containing features found in the earlier stages. Intimal macrophages play a key role in the pathogenesis of atherosclerosis, especially during the initial stages of development [45]. Sub-cellular, punctate THG signal was observed within the intima of mouse (Fig. 1 and 3) and human coronary artery (Fig. 5(b)), near the junction of the media, and appeared similar to small lipid deposits reported within early macrophage foam cells in intimal xanthomas and pathologic intimal thickening [44]. Histological staining in both mouse and human samples confirmed the presence of macrophages in regions with THG structures. The gradual accumulation of lipids within macrophages in accompanied by increased expression of surface scavenger receptors such as CD68 [45]. In both mouse and human, THG puncta also clustered in groups forming patches of 50 – 100 μm. We found CD68-positive macrophages near THG deposits that had similar morphology to these patches. Continual uptake of lipids increases the size of macrophage foam cells leading to the degradation of macrophage cell components and development of extracellular lipids pools [46]. Intermediate lesions and fibrous cap atheromas are identified by extracellular lipid pools within the intima [44], which have a similar morphology to that detected by THG microscopy in some samples (Fig. 3(c)). SHG detected in some regions of plaques (Fig. 4(d) and 5(b)) could be due to accumulated cholesterol crystals. Work by Suhalim and colleagues [47], demonstrated that SHG can arise from chiral cholesterol molecules in the crystal lattice of cholesterol crystals within atherosclerotic plaques. Alternatively, SHG is strongly generated by collagen and advanced lesions consist of fibrous connective tissue primarily composed of collagens overlying a lipid pool [43]. However, SHG detected in these regions did not take the shape of a collagen-rich cap on top of lipid, thus may represent the early stages of collagen deposition.

Biomedical Optics EXPRESS

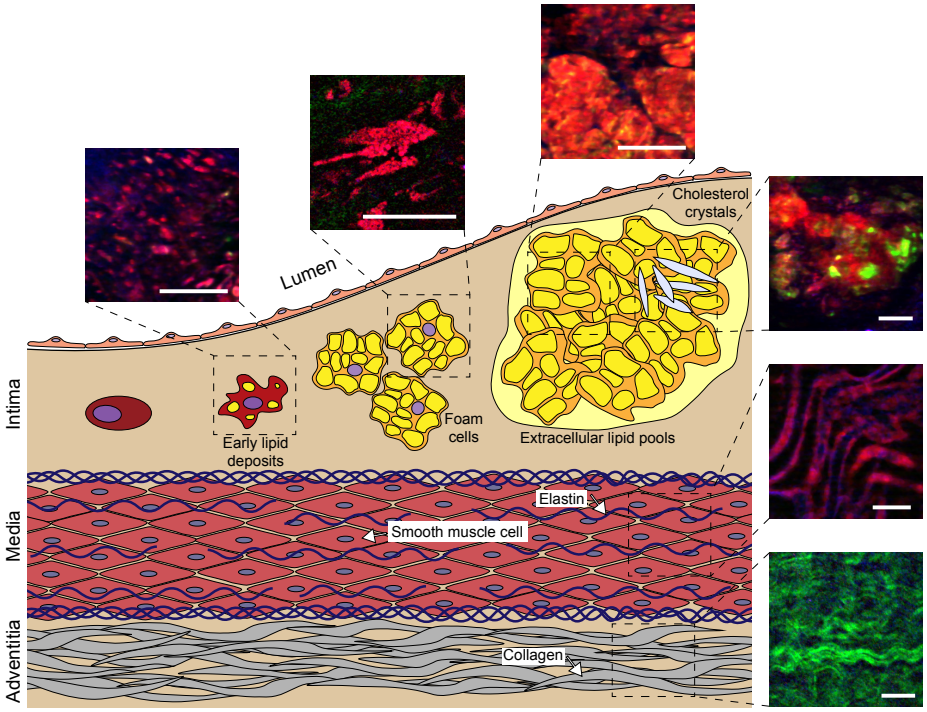

Fig. 6. Summary of morphological features revealed by third harmonic generation (THG) microscopy. Small lipid deposits accumulate in monocytes of the intima during the initial stages of atherosclerosis and can be detected with THG as punctate regions within the intima. Continual uptake of atherogenic lipids increases the size of cellular lipid deposits leading to the formation of foam cells, that are characterized by a cytoplasm filled with lipids. Extracellular lipid pools develop following the breakdown of cellular components and appear with THG imaging as larger regions. Second harmonic generation (SHG) within extracellular lipid pools are most likely cholesterol crystals. Additional nonlinear optical processes simultaneously provide contrast of components of the medial layer (elastin and smooth muscle) and collagens within the adventitia. Red is THG, green is SHG, and blue is autofluorescence. Scale bars are 50 μm.

SHG [48] and 2PEF microscopy [49,50] have previously been used to study atherosclerosis, but imaging with a laser source that enabled efficient higher order nonlinear processes added novel contrast mechanisms. We demonstrated that autofluorescent signals in both rodent and human atherosclerotic samples using MIR excitation showed structures similar to those seen with 2PEF using NIR and therefore can be used to provide anatomical cues and reference points [24,49–51]. Similar to 2PEF, the likely source of autofluorescence within the medial layer of vascular tissue is elastin. Elastin is arranged circumferentially around the vessel lumen in an undulatory pattern [49], has broad emission [24], and the signal matches histology of mouse and human tissue. NADH within smooth muscle cells interspersed with elastin may also contribute to the autofluorescent signal [51]. This source of autofluorescence adds further contrast, aiding the interpretation of atherosclerotic pathology of the vessel wall. For experimental studies of atherosclerosis, exogenous dyes and transgenic rodent models have been used to label structural components and cell types with 2PEF [49,52–54], and may also be used with THG-compatible sources with both two- and three-photon excitation. Previously, two-photon excited autofluorescence of oxidized low-density lipoproteins has been demonstrated and is likely a contributing signal within the atherosclerotic plaque [55]. THG is strongly enhanced at discontinuities in refractive index, so that the strength of the signal in atherosclerotic plaques may in part come from interfaces and structures within the plaques. Some caution is required in interpretation of the THG

Biomedical Optics EXPRESS

signal, because it is not specific only to lipids and the signal from atherosclerotic plaques is likely a combination of THG and fluorescence from various sources [24,55]. Seeger and colleagues used THG to discern tissue morphology in a histological cross-section of human carotid artery atheroma using 1,043 nm excitation [37]. However, this system utilized forward scattering THG signal collection, presumably due to stronger attenuation of the shorter 1,040-nm excitation and the resulting third harmonic, and required a thin 10-μm histological cross-section, rather than the whole tissue preparation used in the current study. The use of higher wavelength excitation at 1,300 nm and 1,700 nm significantly improves the THG signal due to decreased attenuation at these wavelengths. This enables imaging through the vessel wall in both murine and human models which is important for the in vivo use and translatable potential of this technology.

Although there are differences between mouse models and human, we were able to see similar structures in both species [39] which suggests that this imaging modality could be used for label-free imaging in clinical applications. THG microscopy using high peak-power, low repetition-rate lasers may offer an alternate and advantageous approach in the clinical observation of atherosclerosis. Intravascular OCT has had significant adoption for the clinical detection and study of atherosclerosis and can image at sufficient depths (1 – 3 mm) [14–16], however is limited in its diagnostic capabilities to define key plaque features such as lipids, that present as low OCT signal. The capability of OCT to differentiate non-necrotic intracellular and extracellular lipid accumulations from necrotic core lipid remains a challenge [56]. The ability to detect these lipid features would aid the classification of vulnerable lesions. A number of studies have combined OCT with 2PEF of endogenous species, which has improved the structural and molecular analysis of atherosclerotic plaques, often detecting autofluorescence of oxidized lipids within plaques of vulnerable regions [57,58]. While THG-imaging using MIR excitation provides similar information, it does so with enhanced imaging depth that may be needed to assess thicker atheromas which may circumvent the need to combine with another imaging modality. Coherent anti-Stokes Raman (CARS) microscopy has also been shown to be effective at detecting lipid-rich structures [59] including lipids within atherosclerotic plaques and has better chemical specificity than THG since it is based on specific chemical bonds [52,60]. Unfortunately, CARS requires spatial and temporal overlap of two picosecond lasers at different wavelengths [61,62] which remains a technical challenge that limits the widespread uptake of CARS as an in vivo imaging modality. Furthermore, intimal xanthomas represent early vessel pathology [44] that can only be detected microscopically. Study of these lesions are often restricted to post-mortem sampling, therefore a significant void exists in understanding the initiating cell interactions during these early stages in vivo.

Multiphoton microscopy with THG is just one among several technologies which have the potential to study atherosclerosis in vivo. Time-resolved laser-induced fluorescence spectroscopy has been successfully used to detect the biochemical properties of atherosclerotic plaques in patients, cadaveric, and animal samples [63–67]; novel contrast agents such as plasmonic gold nanorods have been used to monitor macrophage distribution in vulnerable plaques [68–70]; and a wide variety of strategies combining different imaging modalities such as OCT, 2PEF, optoacoustic microscopy, and CARS have been used successfully [57,58,71–73]. However, associated toxicities of contrast agents, as well as technical complexity of combining multiple imaging systems, has slowed the practical uptake of new imaging modalities for in vivo detection of atherosclerosis. An imaging modality that utilizes endogenous contrast mechanisms from a single excitation source presents an attractive option for in vivo atherosclerosis imaging.

Although THG imaging has been demonstrated previously, new MIR femtosecond laser sources now make THG imaging feasible for widespread adoption. Advantages of new lasers include a higher peak power, which is critical for higher-order nonlinear excitation, and longer wavelengths, both of which enable greater depth of imaging [74,75]. Laser sources

Biomedical Optics EXPRESS

based on photonic crystal fibers around emitting 1,700 nm have been developed specifically for these applications [76]. Additionally, new and commercially available excitation sources provide turn-key optical parametric amplifiers which allow labs with limited technical knowledge to tune from 1 – 2 μm, that has been unachievable until recently.

THG imaging will likely be readily used in experimental multiphoton microscopy. However, clinical translation will require new advancements to overcome limitations of the current study. This includes the fact that imaging was performed on ex vivo post-fixed tissue under a microscope, and our acquisition scheme was not optimized for intravascular imaging. Improvement in the depth of imaging may also be achievable with currently available methods [74,77,78]. The potential of THG microscopy as a clinical tool depends on the continued progress in development of MIR laser scanning probes [57,58,79–82].

5. Conclusion

New imaging technologies are required that provide high resolution three-dimensional information at sufficient depth to understand and diagnose the heterogeneity of atherosclerosis. Using high peak power, low-repetition laser sources in the MIR range of excitation, it is possible to generate THG from cellular and extracellular lipids in atherosclerotic plaques. Similar studies of atherosclerosis have combined nonlinear optical process (e.g. SHG and endogenous fluorescence) with another imaging modality, such as CARS, to image lipid content. The advantage of the current technique is that the nonlinear optical processes are generated from a single laser source, thereby decreasing the complexity and increasing practicality. THG could be useful for studies that aim to understand the cellular basis for atherosclerosis and lipid deposition. Given the increased practicality of THG imaging and our demonstration of its use in human coronary artery disease, this technique holds potential to be investigated as a clinical tool.

Funding

American Heart Association (13SDG17330004 to NN and 17POST33680127 to DMS), Congressionally Directed Medical Research Program (PR151579P1), New York State Department of Health (DOH01-C32240GG-3450000). Confocal images were acquired at the Cornell BRC-Imaging Facility supported by New York State Stem Cell Science (NYSTEM) (CO29155) and National Institutes of Health (NIH) (S10OD018516).

Acknowledgements

The authors thank Dr. Chris Schaffer and Dr. Chris Xu for assistance and discussion of this project.

Disclosures

The authors declare that there are no conflicts of interest related to this article.